Basal melting of Ross Ice Shelf from solar heat absorption in an ice-front polynya

Craig L. Stewart [1,2]*, Poul Christoffersen [1], Keith W. Nicholls [3], Michael J. M. Williams[2] and Julian A. Dowdeswell[1]

Ice–ocean interactions at the bases of Antarctic ice shelves are rarely observed, yet have a profound influence on ice sheet evolution and stability. Ice sheet models are highly sensitive to assumed ice shelf basal melt rates; however, there are few direct observations of basal melting or the oceanographic processes that drive it, and consequently our understanding of these interactions remains limited. Here we use in situ observations from the Ross Ice Shelf to examine the oceanographic processes that drive basal ablation of the world's largest ice shelf. We show that basal melt rates beneath a thin and structurally important part of the shelf are an order of magnitude higher than the shelf-wide average. This melting is strongly influenced by a seasonal inflow of solar-heated surface water from the adjacent Ross Sea Polynya that downwells into the ice shelf cavity, nearly tripling basal melt rates during summer. Melting driven by this frequently overlooked process is expected to increase with predicted surface warming. We infer that solar heat absorbed in ice-front polynyas can make an important contribution to the present-day mass balance of ice shelves, and potentially impact their future stability.

The ice shelves that fringe Antarctica interact with the Southern Ocean across a basal surface of 1.56×10^6 km[21]. Melting of this vast surface is the single largest cause of mass loss from the Antarctic Ice Sheet[1,2]. Thinning induced by ice shelf basal melting can also modify inland ice flow, reducing the stabilizing effect of sills, shoals and sidewalls[3,4] and in some cases driving instantaneous dynamic responses as far as 900 km inland[4]. Although these processes provide a primary control on the future evolution of the ice sheet[3,5], there are still relatively few direct observations of basal melting and oceanographic conditions within ice shelf cavities[6], and this paucity of data impedes the development of theory and models.

In Antarctic shelf seas, three main water masses are thought to influence ice shelves[7]: Circumpolar Deep Water (CDW), a relatively warm water mass that surrounds Antarctica at intermediate depth; high and low salinity shelf water (HSSW and LSSW), which is formed as the sea surface freezes during winter; and Antarctic Surface Water (AASW), a relatively fresh and buoyant water mass influenced by solar heating and sea ice melting during summer[8].

These water masses have contrasting impacts on ice shelves. CDW in the Amundsen Sea has caused ice shelves in the region to thin over recent decades[9,10] driving mass loss from the interior ice sheet[11,12]. In contrast, the vast Ross and Filchner-Ronne ice shelves seem to be near equilibrium[13,14], due to the presence of cold shelf waters that limit their exposure to CDW[8,15,16]. The influence of AASW on ice shelves is less clear and seldom considered. Although buoyant, AASW can enter ice shelf cavities due to wind[17,18] and tidal forcing[19–21]; however, observations of AASW beneath ice shelves have only been made recently[22,23], and few studies have examined this process in detail.

Recent satellite observations of the Ross Ice Shelf (RIS), which at 500,809 km[2](ref.[1]) accounts for 32% of Antarctica's total ice shelf area, suggest relatively low shelf-wide mean basal melt rates of 0.07 to 0.11 m yr[−1](refs.[1,2,24]). However, these studies also indicate rates above 1 m yr^{−1} in the north-western sector of the shelf[1,24]. Although remote-sensing estimates have uncertainties of over 100% (ref.[24]),

earlier glaciological observations[25–27] and oceanographic models[23,28–31] also indicate rapid melting in the north-western RIS. These models suggest that active circulation of frontal water into the cavity during summer and low-frequency flow variability may influence this region. Isolated observations from beneath the ice shelf support this picture[23,31], yet the details of these processes and the magnitude of their impact on the ice shelf remain unclear.

Here we present in situ observations of basal melting and sub-ice shelf oceanographic conditions from the north-western RIS. The aims of the study are two-fold: to quantify and map basal melting in the region surrounding Ross Island, and to examine the role of surface water in driving this process.

Radar mapping of basal melting. We used a downward-looking phase-sensitive radio echo sounder[32,33] to make precise measurements at 78 sites surrounding Ross Island (Fig. 1) to quantify basal melting of the north-western RIS. All sites were resurveyed after 1 yr, allowing annual mean melt rates to be calculated (see Methods and Supplementary Table 1). Further observations were used to determine short-term summer melt rates near the ice front (Supplementary Table 2). The melt rate observations were interpolated onto a regular grid to map the melt rate field and estimate the total basal mass loss from the region (see Methods).

The observations show intense basal melting within 1 km of the ice shelf front, with annual mean rates of 2.4–7.7 m yr^{−1} in this zone (Fig. 1). Melt rates reduce exponentially with distance from the ice front, typically halving within the frontal 3 km (Fig. 1b). This pattern is consistent with trends inferred from laser altimetry[34], but our observations show higher melt rates and reveal small-scale spatial variability.

The melt rate observations indicate strong seasonal melt rate variability, with rapid summer melting especially pronounced near the ice front and on Transect TC (Fig. 1c). Here, a maximum ablation of 0.714 ± 0.007 m was recorded over a 4.89 d period during January 2013, indicating a melt rate of 0.146 m d^{−1} (53 m yr^{−1};
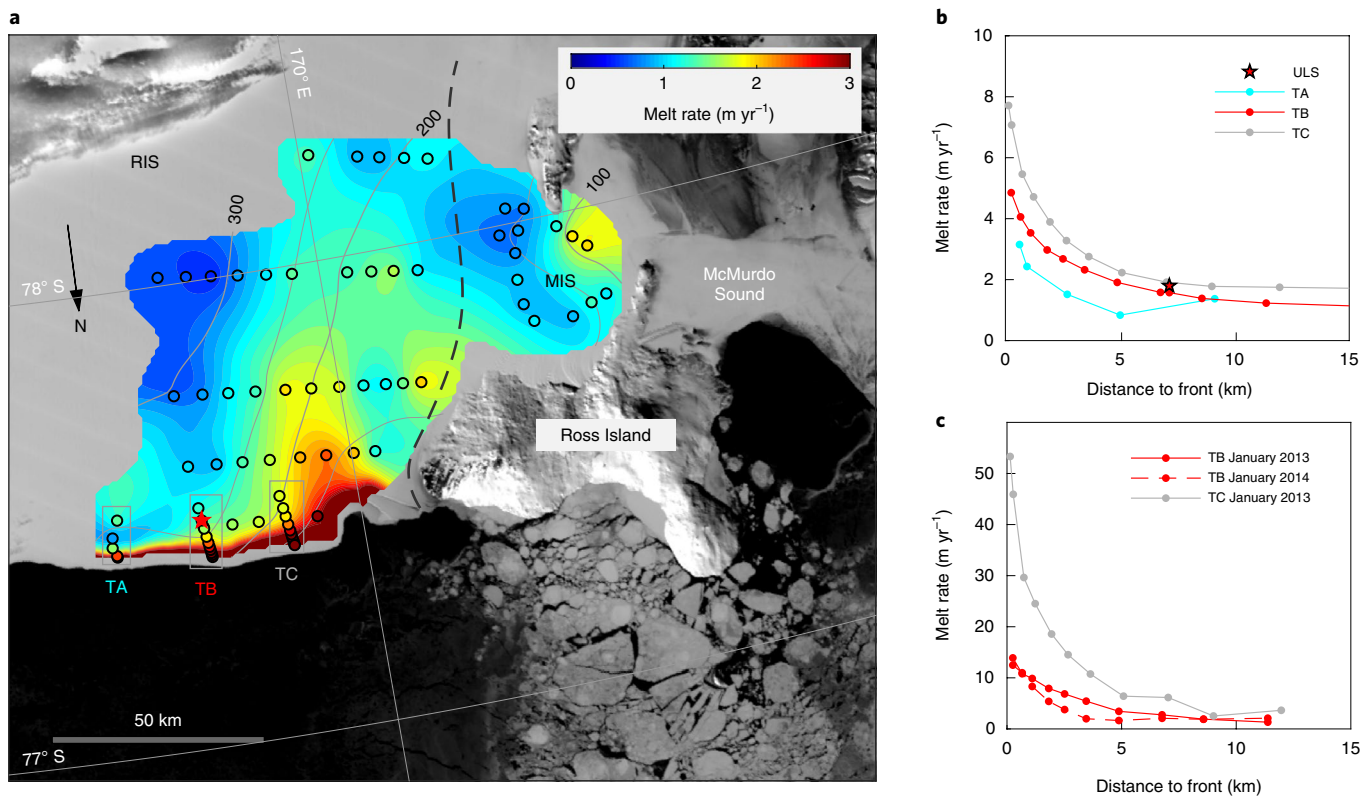
Fig. 1 | Basal melt rates of the north-western RIS. a, Annual mean basal melt rate observations (coloured dots) and the interpolated melt rate field (shaded region) are shown, with the mooring location (red star) and Transects TA–TC. Grey boxes indicate sites within transects. The ice thickness (in m, grey contours) and the shear zone that separates the RIS and MIS (dashed black line) are also shown. The background MODIS image is from 10 November 2015[54]. **b,c**, Annual mean (**b**) and short-term summer (**c**) melt rates for frontal transects TA–TC. The mean melt rate from the moored Upward Looking Sonar (see Oceanographic observations) is indicated by the red star in **b**. Credit (basemap in **a**): ref. [54], NSIDC.

Supplementary Table 2). This rate is a factor of 6.9 higher than the annual mean rate at the same site, suggesting that a large component of the net ablation occurs in summer.

Melt rates are lower beyond the frontal 15 km, yet still considerably above the shelf-wide average of ~0.1 m yr⁻¹(refs. [1,2,24]). The pattern of melting implies that the net heat flux into the cavity is strongest ~20 km east of Ross Island, near an embayment where frontal ice thickness reduces to approximately 100 m (ref. [35]). In this area, rapid melting extends further from the ice front (Fig. 1a). The mean basal melt rate across the 7,782 km² interpolated area is 1.34 m yr⁻¹, indicating a basal mass loss of 9.5 Gt yr⁻¹. This represents 20% of the published net basal mass loss from the entire RIS[1] from just 1.6% of its area.

The rapid frontal melting and the large seasonal variations in melt rates suggest that melting near the ice front may be influenced by an inflow of warm surface water during summer, as observed beneath McMurdo Ice Shelf (MIS)[23]. As warm inflowing water is expected to progressively cool through contact with the ice base, this mechanism could also explain the exponential reduction in melt rate with frontal distance.

Oceanographic observations. To examine the oceanographic processes that drive enhanced melting in the north-western sector of RIS, a sub-ice shelf mooring was deployed 7 km from the ice front on Transect TB (Fig. 1a). Moored instruments recorded currents, temperature and salinity hourly for up to 4 yr. An upward-looking sonar (ULS) was also deployed beneath the ice base, allowing basal melt rates to be determined (see Methods).

Currents at the mooring site show strong seasonal variability, with mean depth-averaged outflows during winter (April–November)

and inflows during late summer (February–March) (Fig. 2a). The strength and duration of this inflow imply ventilation of the outer ~50–160 km of the cavity. A comparison of water temperature at the mooring with sea surface temperature (SST)[36] north of the ice front suggests that the inflow has a direct impact on temperatures in the cavity (Fig. 2c). Averaged over the region within 100 km of the mooring, SST follows an annual cycle that is closely linked to mean sea-ice concentration in the same region (Fig. 2c). Here temperatures vary from the surface freezing point during winter to seasonal maxima of over 1 °C in January, when sea ice is absent. Temperatures measured ~13 m below the ice base at the mooring show a similar but delayed and attenuated cycle, with seasonal maxima occuring in February, approximately one month after the SST peak.

Further clues to the origin of the warm inflow are provided by a single serendipitous conductivity temperature depth (CTD) cast, sampled 120 km north of the mooring site (Fig. 2a) 1 d before mooring deployment[37]. This cast shows a 40-m-thick, relatively fresh upper layer with a surface temperature of 0.178 °C (Fig. 2b). The 0.8 °C temperature range of the upper 35 m is associated with a salinity range of just 0.009 psu, suggesting solar heating of a previously homogenous layer. Comparison of the CTD cast with temperature–salinity (T–S) observations from the upper moored sensor, located 8 m below the ice base (~229 m below sea level), suggests that surface water is drawn into the cavity. By extending the extrema of the offshore CTD cast with 2.4 °C psu⁻¹ meltwater mixing lines[16,38], we define an envelope of water masses that could be formed from the offshore water by interaction with the ice shelf. Throughout January and February 2011, all 863 observations from the upper sub-ice shelf T–S sensor fall within this envelope (Fig. 2b). The sub-ice shelf observations are consistent with a source region in the offshore
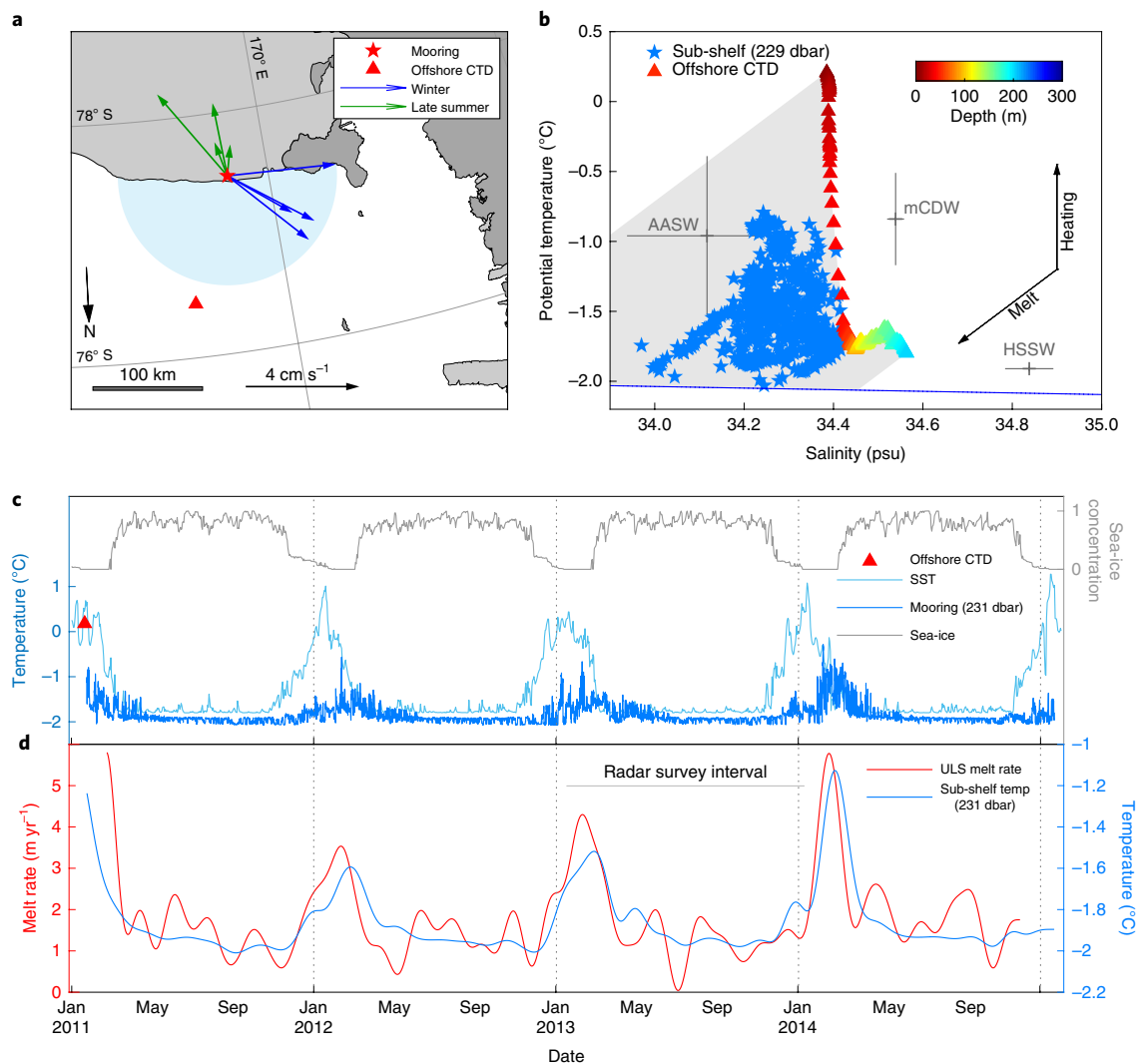
Fig. 2 | Oceanographic conditions and melt rate variability. a, Depth-averaged flow at the mooring site for winter (May–November) and late summer (February–March) for calendar years 2011–2014. The mooring site, the RV *Nathaniel B. Palmer* offshore CTD cast[37] and the region within 100 km of the mooring used to average SST and sea-ice concentration (light blue shading) are also shown. **b**, *T–S* observations from the offshore CTD cast (colour scale) and from the highest sub-ice shelf *T–S* sensor, located ~8 m below the ice base. The in situ freezing point at the ice base (blue line), representative water properties of HSSW, modified CDW (mCDW) and AASW[55] are shown, as are water masses that may be derived from the offshore surface layer through interaction with the ice shelf (grey shading). Arrows indicate the *T–S* evolution associated with solar heating and ice melt. **c**, Mean SST[36] (left *y* axis) and sea-ice concentration[42,56] (right *y* axis) within 100 km of the mooring (see Methods). The temperature measured ~13 m below the ice base and SST from the offshore CTD cast are also plotted. **d**, ULS basal melt rates (left *y* axis) and low-pass filtered sub-ice shelf water temperature (right *y* axis). Credit (basemap in **c**): https://www.add.scar.org/.

profile above 55 m, indicating that the surface layer downwells to reach the mooring site. The characteristics of the warmest sub-ice shelf water are consistent with the mean properties of the upper ~50 m of the offshore profile, suggesting that the surface layer is homogenized before reaching the mooring.

The impact of water temperature variability on the ice shelf is illustrated by comparing the ULS basal melt rate record with water temperature from the upper moored current meter (Fig. 2d). Both records are low-pass filtered (cutoff frequency $f_c = 0.02$ cycle d^{-1}) to reduce the impact of noise in the range observations (see Methods). The dominant feature of the melt rate record is a strong seasonal cycle that peaks in February. The smoothed temperature and melt rate records are highly correlated (Pearson's $r = 0.78$), indicating that water temperature is the dominant driver of low-frequency melt rate variability at the mooring site.

The mean ULS melt rate for the central 3-yr period June 2011–May 2014 is 1.8 m yr^{-1} (Fig. 1b). Seasonally, melt rates vary between

1.1 m yr^{-1} during late winter (September–November) when sub-ice shelf water temperatures are at or below the surface freezing point, and 3.0 m yr^{-1} during summer (January–March) when surface water is seen at the site. This rapid melting occurs over a relatively short period, and the difference between the late-winter and annual mean rates implies that summer melting accounts for ~0.7 m yr^{-1}, or 40% of net ablation at the mooring site. Determining the contribution of surface water to net ablation over the wider survey region is more difficult due to the lack of winter melt rate observations away from the mooring site. However, the higher summer/annual mean melt rate ratios seen on Transect TC, 20 km west of the mooring (Fig. 1b,c and Supplementary Table 2) suggest that the influence of surface water is stronger here.

Although melt rates peak during February, winter rates are still an order of magnitude higher than the satellite-inferred shelf-wide average, and contribute substantially to the high average melt rates. This indicates that either winter current speeds or water
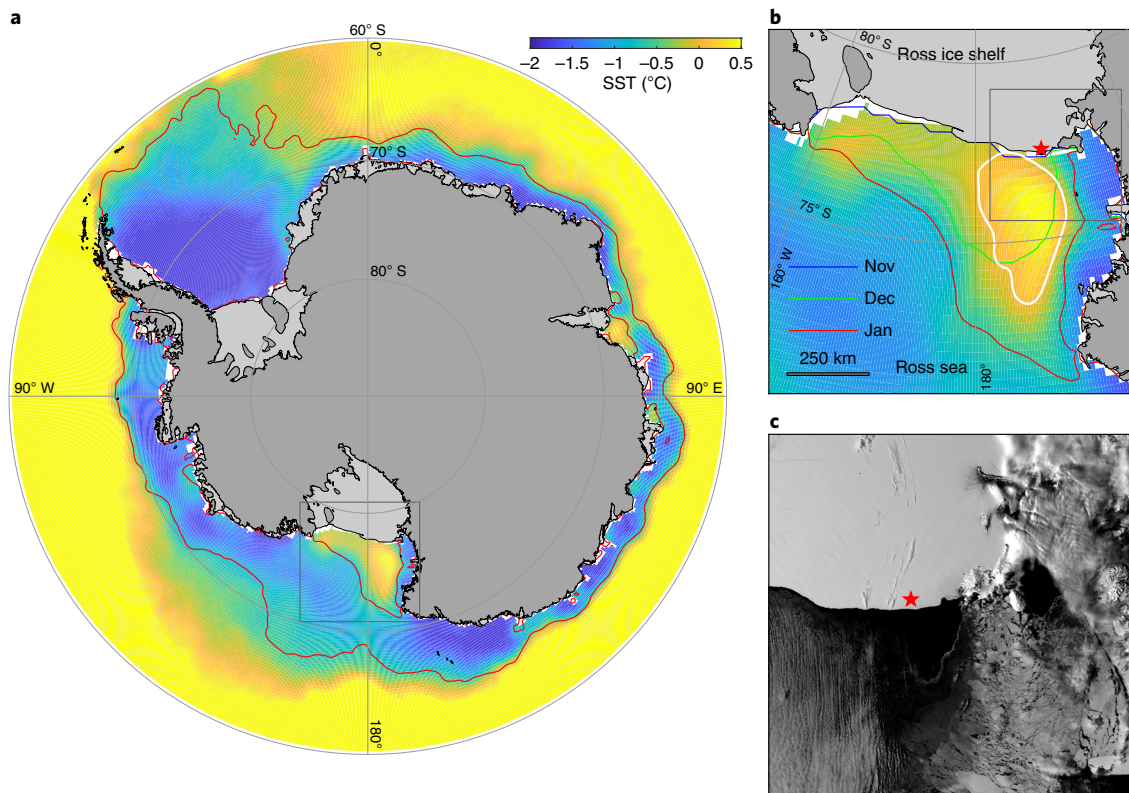
Fig. 3 | SST and sea-ice concentration around Antarctica. a, Long-term mean January SST[36] (colour scale) with the 15% sea ice concentration[42,56] contour (red) (see Methods). **b**, Close-up map of the Ross Sea showing the January mean 0 °C SST isotherm (white) and the 15% sea-ice concentration contours for November and December. **c**, MODIS image taken during strong southerly airfow on 12 November 2015[54]. Grey boxes in **a** and **b** indicate the regions shown in **b** and **c**, respectively. The red star indicates the mooring location. Credit (basemap): https://www.add.scar.org (**a,b**); ref. [54], NSIDC (**c**).

temperatures at the mooring are higher than the shelf-wide average. Although localized flow enhancement may contribute to rapid melting in the region, it seems unlikely that this could explain the enhancement of melt rates by an order of magnitude, and we suggest that temperature variability plays the dominant role. There are few observations from elsewhere in the cavity, but CTD profiles from the central RIS show a thick Ice Shelf Water (defined water mass, below surface freezing point; see ref. [15]) boundary layer within 0.03 °C of the in situ freezing point[39]. In contrast, water near the ice base at the mooring site is often above the surface freezing point during early winter, indicating remnant heat from the summer inflow. Even during late winter, HSSW 0.17 °C above the in situ freezing point is frequently observed, and this suggests active cross-frontal flow that ventilates the cavity[40,41].

Surface ocean heat. The identification of a warm surface water inflow that drives rapid basal melting raises crucial questions: what is origin of this heat, and could this process influence other ice shelves? To address these questions, we examine summer SST and sea-ice concentration observations from coastal Antarctica.

Figure 3a shows long-term mean January SST[36] and sea-ice distribution, represented here by the mean 15% sea-ice concentration contour[42] (see Methods). At the largest scale, summer SST is inversely correlated with sea-ice concentration and the coldest waters are typically found near the coastline (Fig. 3a). However, higher temperatures are observed where sea ice is absent, including coastal polynyas near the RIS and Amery Ice Shelf (see also ref. [43]).

Within the Ross Sea, SST variability is dominated by a warm surface anomaly, previously identified in CTD observations[44], that closely matches the position of the Ross Sea Polynya (Fig. 3b). In this region, January mean SST reaches ~0.5 °C. This pattern of

warming is consistent with atmospheric modelling that indicates that Antarctic polynyas absorb solar heat rapidly during summer[45], and has previously been attributed to summer insolation in the Ross Sea Polynya[23,46].

To assess whether the warm surface pool evident in Fig. 3b could supply the energy required for elevated melting in the survey region, we calculated the available thermal energy within its surface waters during January (see Methods). Considering the region within the 0 °C SST isotherm (Fig. 3b), and assuming a surface mixed layer depth of 10 m, provides a sensible heat content of 8.3×10^{18} J, sufficient to melt 22 Gt of the ice shelf. This is approximately twice the observed mass loss within the survey region. Despite uncertainty in the mixed layer depth, surface waters in the Ross Sea clearly represent a glaciologically important heat reservoir during summer.

Beyond the Ross Sea, coastal SSTs above −0.5 °C are only seen in the north-western Antarctic Peninsula, where the sea-ice concentration is low, and in the polynya adjacent to the eastern Amery Ice Shelf (Fig. 3a). Consequently, although surface layer heat may affect these regions, this process does not seem to be widespread at present.

Drivers and impacts of surface water inflow. Although surface waters have been considered a potential driver of ice shelf basal melting for some time[7,22–24], the observations presented here provide detailed evidence of this process. These data suggest that solar-heated surface water contributes substantially to the basal mass balance of the RIS, and that surface water plays a larger role in the mass balance of ice shelves than previously assumed.

In the north-western Ross Sea, the impact of surface water can be attributed to two processes; localized solar heating of the surface ocean during summer, and transport of this energy into the cavity by a seasonal inflow. Surface heating seems to be closely linked to

the consistent wind-driven expansion of the Ross Sea Polynya in spring[23,46]. During this period, sustained southerly winds (guided by the Transantarctic Mountains) preferentially export sea ice from the western ice front[47,48]. As air temperatures and insolation increase throughout November and December, the polynya expands rapidly (Figs. 2c and 3b), as illustrated by the sea-ice distribution during this period (Fig. 3c). This process increases the absorption of solar energy in the surface layer, and removes the latent heat sink presented by sea ice, aiding rapid heating of the surface layer (Fig. 2c).

The drivers of the late-summer inflow are less obvious. However, due to the buoyancy of the surface layer, it seems likely that external forcing is required. In contrast to the wind-driven downwelling observed elsewhere[18], the inflow observed here is not associated with downwelling-favourable winds. Modelling suggests that circulation near and beneath the ice shelf is strongly influenced by density gradients caused by seasonal brine release in the polynya[41] and that these circulation patterns influence seasonal flow variability near Ross Island[28]. Considering these factors, we conclude that the elevated melt rates in the north-western RIS are linked to the location of Ross Sea Polynya, and ultimately the mean winds and orography of the region.

The identification of surface layer heat as a driver of basal melting of the RIS has several important implications. First, as heat absorption within the polynya is controlled by atmospheric processes[45], basal mass balance in the frontal zone of the ice shelf is likely to vary with atmospheric and surface ocean conditions near the ice front on seasonal, interannual and longer-term timescales. Considering that summer sea-ice concentrations in the Ross Sea are projected to decrease by 56% by 2050[49], and that the ice-free period is also expected to increase[50], it seems likely that ice-shelf basal melting in this region will also increase rapidly. If surface warming and sea-ice loss are widespread, this process may also become more widespread. Second, AASW drives a mode of basal ablation that is distinct from that of denser water masses, and these differences have implications for ice shelf stability. For example, whereas meltwater derived from HSSW can refreeze in shallower regions, potentially stabilizing ice shelves[51], meltwater formed from AASW is unlikely to be redeposited due to its relative warmth. Furthermore, the influence of surface water is greatest in frontal regions. Although some frontal regions are unimportant to the stability of ice shelves, others contain critical pinning points that sustain the location of the front[52,53]. Ross Island seems to be one such pinning point, and recent modelling shows that the rapid melting identified here influences a structurally critical region in which ice thickness changes can influence the flow speed of the entire ice shelf[4].

The exposure of this sensitive part of the ice shelf to surface ocean heat implies that the grounding line flux of the entire ice shelf may be modulated at seasonal to interannual timescales by surface water inflow. This process represents a frequently overlooked, but potentially important, factor in regional ice-shelf mass balance and should be considered in future assessments of ice shelf stability.

Online content

Any methods, additional references, Nature Research reporting summaries, source data, extended data, supplementary information, acknowledgements, peer review information; details of author contributions and competing interests; and statements of data and code availability are available at https://doi.org/10.1038/s41561-019-0356-0.

References

1. Rignot, E., Jacobs, S., Mouginot, J. & Scheuchl, B. Ice-shelf melting around Antarctica. *Science* **341**, 266–270 (2013).
2. Depoorter, M. et al. Calving fluxes and basal melt rates of Antarctic ice shelves. *Nature* **502**, 89–92 (2013).
3. Arthern, R. J. & Williams, C. R. The sensitivity of West Antarctica to the submarine melting feedback. *Geophys. Res. Lett.* **44**, 2352–2359 (2017).
4. Reese, R., Gudmundsson, G. H., Levermann, A. & Winkelmann, R. The far reach of ice-shelf thinning in Antarctica. *Nat. Clim. Change* **8**, 53–57 (2018).
5. Pattyn, F. Sea-level response to melting of Antarctic ice shelves on multi-centennial timescales with the fast Elementary Thermomechanical Ice Sheet model (f.ETIShv1.0). *Cryosphere* **11**, 1851–1878 (2017).
6. Jenkins, A., Nicholls, K. W. & Corr, H. F. J. Observation and parameterization of ablation at the base of Ronne Ice Shelf, Antarctica. *J. Phys. Oceanogr.* **40**, 2298–2312 (2010).
7. Jacobs, S., Hellmer, H., Doake, C., Jenkins, A. & Frolich, R. Melting of ice shelves and the mass balance of Antarctica. *J. Glaciol.* **38**, 375–387 (1992).
8. Orsi, A. H. & Wiederwohl, C. L. A recount of Ross Sea waters. *Deep Sea Res. Pt II* **56**, 778–795 (2009).
9. Jenkins, A. et al. Observations beneath Pine Island Glacier in West Antarctica and implications for its retreat. *Nat. Geosci.* **3**, 468–472 (2010).
10. Paolo, F. S., Fricker, H. A. & Padman, L. Volume loss from Antarctic ice shelves is accelerating. *Science* **348**, 327–331 (2015).
11. Velicogna, I., Sutterley, T. & Van Den Broeke, M. Regional acceleration in ice mass loss from Greenland and Antarctica using GRACE time-variable gravity data. *Geophys. Res. Lett.* **41**, 8130–8137 (2014).
12. Shepherd, A. et al. Mass balance of the Antarctic ice sheet from 1992 to 2017. *Nature* **556**, 219–222 (2018).
13. Shepherd, A. et al. Recent loss of floating ice and the consequent sea level contribution. *Geophys. Res. Lett.* **37**, L13503 (2010).
14. Pritchard, H. et al. Antarctic ice-sheet loss driven by basal melting of ice shelves. *Nature* **484**, 502–505 (2012).
15. Jacobs, S. S., Amos, A. F. & Bruchhausen, P. M. Ross Sea oceanography and Antarctic Bottom Water formation. *Deep Sea Res. Oceanogr. Abstr.* **17**, 935–962 (1970).
16. Nicholls, K. W., Østerhus, S., Makinson, K., Gammelsrød, T. & Fahrbach, E. Ice-ocean processes over the continental shelf of the southern Weddell Sea, Antarctica: a review. *Rev. Geophys.* **47**, RG3003 (2009).
17. Sverdrup, H. U. The currents off the coast of Queen Maud Land. *Norsk Geogr. Tidssk.* **14**, 239–249 (1954).
18. Zhou, Q. et al. Wind-driven spreading of fresh surface water beneath ice shelves in the Eastern Weddell Sea. *J. Geophys. Res. Oceans* **119**, 3818–3833 (2014).
19. Gammelsrod, T. & Slotsvik, N. Hydrographic and current measurements in the southern Weddell Sea 1979/80. *Polarforschung* **51**, 101–111 (1981).
20. Jenkins, A. & Doake, C. S. M. Ice-ocean interaction on Ronne Ice Shelf, Antarctica. *J. Geophys. Res.* **96**, 791–813 (1991).
21. Makinson, K. & Nicholls, K. W. Modeling tidal currents beneath Filchner-Ronne Ice Shelf and on the adjacent continental shelf: their effect on mixing and transport. *J. Geophys. Res. Oceans* **104**, 13449–13465 (1999).
22. Hattermann, T., Nøst, O. A., Lilly, J. M. & Smedsrud, L. H. Two years of oceanic observations below the Fimbul Ice Shelf, Antarctica. *Geophys. Res. Lett.* **39**, L12605 (2012).
23. Stern, A. A., Dinniman, M. S., Zagorodnov, V., Tyler, S. W. & Holland, D. M. Intrusion of warm surface water beneath the McMurdo Ice Shelf, Antarctica. *J. Geophys. Res. Oceans* **118**, 7036–7048 (2013).
24. Moholdt, G., Padman, L. & Fricker, H. A. Basal mass budget of Ross and Filchner-Ronne ice shelves, Antarctica, derived from Lagrangian analysis of ICESat altimetry. *J. Geophys. Res. Earth* **119**, 2361–2380 (2014).
25. Crary, A., Robinson, E., Bennett, H. & Boyd, W. Glaciological regime of the Ross Ice Shelf. *J. Geophys.* **67**, 2791–2807 (1962).
26. Neal, C. The dynamics of the Ross Ice Shelf revealed by radio echo-sounding. *J. Glaciol.* **24**, 295–307 (1979).
27. Bamber, J. & Bentley, C. A comparison of satellite-altimetry and ice-thickness measurements of the Ross Ice Shelf, Antarctica. *Ann. Glaciol.* **20**, 357–364 (1994).
28. Assmann, K., Hellmer, H. H. & Beckmann, A. Seasonal variation in circulation and water mass distribution on the Ross Sea continental shelf. *Antarct. Sci.* **15**, 3–11 (2003).
29. Holland, D. M., Jacobs, S. S. & Jenkins, A. Modelling the ocean circulation beneath the Ross Ice Shelf. *Antarct. Sci.* **15**, 13–23 (2003).
30. Dinniman, M. S., Klinck, J. M. & Smith, W. O. Influence of sea ice cover and icebergs on circulation and water mass formation in a numerical circulation model of the Ross Sea, Antarctica. *J. Geophys. Res.* **112**, C11013 (2007).
31. Arzeno, I. B. et al. Ocean variability contributing to basal melt rate near the ice front of Ross Ice Shelf, Antarctica. *J. Geophys. Res. Oceans* **119**, 4214–4233 (2014).
32. Brennan, P. V., Nicholls, K., Lok, L. B. & Corr, H. Phase-sensitive FMCW radar system for high-precision Antarctic ice shelf profile monitoring. *IET Radar Sonar Navig.* **8**, 776–786 (2014).

33. Nicholls, K. W. et al. A ground-based radar for measuring vertical strain rates and time-varying basal melt rates in ice sheets and shelves. *J. Glaciol.* **61**, 1079–1087 (2015).

34. Horgan, H. J., Walker, R. T., Anandakrishnan, S. & Alley, R. B. Surface elevation changes at the front of the Ross Ice Shelf: implications for basal melting. *J. Geophys. Res.* **116**, C02005 (2011).

35. Griggs, J. & Bamber, J. Antarctic ice-shelf thickness from satellite radar altimetry. *J. Glaciol.* **57**, 485–498 (2011).

36. *GHRSST Level 4 MUR Global Foundation Sea Surface Temperature Analysis* v.2 (JPL MUR MEaSUREs Project, accessed 8 July 2018); https://doi.org/10.5067/GHGMR-4FJ01

37. Kohut, J. *Calibrated Hydrographic Data from the Ross Sea Acquired with a CTD During the* Nathaniel B. Palmer *Expedition NBP1101* (MGDS, accessed 27 August 2011); https://doi.org/10.1594/ieda/317595

38. Gade, H. G. Melting of ice in sea water: a primitive model with application to the Antarctic ice shelf and icebergs. *J. Phys. Oceanogr.* **9**, 189–198 (1979).

39. Gilmour, A. E. Ross Ice Shelf sea temperatures. *Science* **203**, 438–439 (1979).

40. Årthun, M., Holland, P. R., Nicholls, K. W. & Feltham, D. L. Eddy-driven exchange between the open ocean and a sub–ice shelf cavity. *J. Phys. Oceanogr.* **43**, 2372–2387 (2013).

41. Jendersie, S., Williams, M. J., Langhorne, P. J. & Robertson, R. The density-driven winter intensification of the Ross Sea circulation. *J. Geophys. Res. Oceans* **123**, 7702–7724 (2018).

42. Meier, W. et al. *NOAA/NSIDC Climate Data Record of Passive Microwave Sea Ice Concentration* v.3 (NOAA/NSIDC, accessed 7 March 2019); https://doi.org/10.7265/N59P2ZTG

43. Ohshima, K. I., Nihashi, S. & Iwamoto, K. Global view of sea-ice production in polynyas and its linkage to dense/bottom water formation. *Geosci. Lett.* **3**, 1–14 (2016).

44. Smethie, W. M. Jr. & Jacobs, S. S. Circulation and melting under the Ross Ice Shelf: estimates from evolving CFC, salinity and temperature fields in the Ross Sea. *Deep Sea Res. Pt I* **52**, 959–978 (2005).

45. Renfrew, I. A., King, J. C. & Markus, T. Coastal polynyas in the southern Weddell Sea: variability of the surface energy budget. *J. Geophys. Res. Oceans* **107(C6)**, 16-1–16-22 (2002).

46. Jacobs, S. S. & Comiso, J. C. Sea ice and oceanic processes on the Ross Sea continental shelf. *J. Geophys. Res. Oceans* **94**, 18195–18211 (1989).

47. Bromwich, D. H., Carrasco, J. F., Liu, Z. & Tzeng, R.-Y. Hemispheric atmospheric variations and oceanographic impacts associated with katabatic surges across the Ross Ice Shelf, Antarctica. *J. Geophys. Res. Atmos.* **98**, 13045–13062 (1993).

48. Comiso, J. C., Kwok, R., Martin, S. & Gordon, A. L. Variability and trends in sea ice extent and ice production in the Ross Sea. *J. Geophys. Res.* **116**, C04021 (2011).

49. Smith, W. O., Dinniman, M. S., Hofmann, E. E. & Klinck, J. M. The effects of changing winds and temperatures on the oceanography of the Ross Sea in the 21st century. *Geophys. Res. Lett.* **41**, 1624–1631 (2014).

50. Dinniman, M. S., Klinck, J. M., Hofmann, E. E. & Smith, W. O. Effects of projected changes in wind, atmospheric temperature, and freshwater inflow on the Ross Sea. *J. Climate* **31**, 1619–1635 (2018).

51. Jansen, D., Luckman, A., Kulessa, B., Holland, P. R. & King, E. C. Marine ice formation in a suture zone on the Larsen C Ice Shelf and its influence on ice shelf dynamics. *J. Geophys. Res. Earth* **118**, 1628–1640 (2013).

52. Doake, C., Corr, H., Rott, H., Skvarca, P. & Young, N. Breakup and conditions for stability of the northern Larsen Ice Shelf, Antarctica. *Nature* **391**, 778–780 (1998).

53. Fürst, J. J. et al. The safety band of Antarctic ice shelves. *Nat. Clim. Change* **6**, 479–482 (2016).

54. Scambos, T., Bohlander, J. & Raup, B. *Images of Antarctic Ice Shelves, Version 1: West Ross Ice Shelf* (National Snow and Ice Data Center, 1996); https://doi.org/10.7265/N5NC5Z4N

55. Jacobs, S. S., Fairbanks, R. G. & Horibe, Y. *Origin and Evolution of Water Masses Near the Antarctic Continental Margin: Evidence from $H_2^{18}O/H_2^{16}O$ Ratios in Seawater* 59–85 (American Geophysical Union, 1985).

56. Peng, G., Meier, W. N., Scott, D. J. & Savoie, M. H. A long-term and reproducible passive microwave sea ice concentration data record for climate studies and monitoring. *Earth System Sci. Data* **5**, 311–318 (2013).

Author contributions
C.L.S. and M.J. M.W. designed and deployed the sub-ice shelf mooring. C.L.S. designed the radar survey, and C.L.S. and P.C. undertook the radar fieldwork. C.L.S. analysed the radar data with advice from K.W.N. All authors contributed to the manuscript.

Competing interests
The authors declare no competing interests.

Additional information
Supplementary information is available for this paper at https://doi.org/10.1038/s41561-019-0356-0.

Reprints and permissions information is available at www.nature.com/reprints.

Correspondence and requests for materials should be addressed to C.L.S.

Publisher's note: Springer Nature remains neutral with regard to jurisdictional claims in published maps and institutional affiliations.

Methods

Radar observations. Basal melt rates were measured using the British Antarctic Survey's autonomous phase-sensitive radio echosounder (ApRES)[33]. This frequency-modulated continuous-wave radar has a centre frequency of 300 MHz and bandwidth of 200 MHz. The instrument uses direct digital synthesis to generate the linear 1 s chirp, and demodulates the radio-frequency carrier wave by mixing the receive signal with an attenuated feed of the transmit signal. The resulting audio-frequency signal is digitized at 40 kHz. The same high-stability master clock is used to drive both signal generation and sampling, ensuring precise synchronization. Technical details of the instrument are given in ref.[32].

The instrument was used in a pseudo-monostatic configuration, with the transmit and receive antennas separated by 3.44 m. At each site an ensemble (burst) of typically 100 chirps was recorded. Radar sites were marked with surface stakes to ensure that the same column of ice was sampled on each visit. Care was taken to ensure precise relocation of the instrument relative to the marks, and the repositioning error was estimated to be <0.05 m.

Data from each visit to each site were preprocessed as follows. For each burst, noisy chirps were removed, and the remaining chirps averaged. Each burst-mean chirp was weighted with a Blackman window, then extended to a multiple of 8 times its original length by appending trailing zeros. Following this zero-padding, the signal was circularly rotated so that the first sample of the modified signal was that of the centre of the unpadded chirp (see ref.[57]). Each chirp was then Fourier transformed.

Due to the frequency-range proportionality in linear frequency-modulated continuous-wave radar observations[32], the amplitude of the resulting spectrum is analogous to a time series of echo amplitude recorded by a time-domain radar. These complex valued spectra are hereafter referred to as profiles. Without zero-padding, the profiles have a frequency resolution of 1 Hz, and the 200 MHz bandwidth implies a temporal resolution of 5 ns, corresponding to a range resolution of 0.43 m in ice. With zero-padding, the interpolated range resolution is 0.0537 m. Here and in the following analysis we assume a nominal propagation velocity of 1.68×10^8 m s^{-1} (ref.[58]).

Although changes in the range of the basal reflector are relatively simple to determine, these are influenced by many factors including changes in radar hardware (for example cable length), compaction of the upper snow layers (firn), strain within the solid ice and basal melting. To isolate the component due to basal melting, observations of internal reflector displacement were used to tune a displacement model. This model was used to estimate the displacement of the ice base expected in the absence of basal melting. Net basal ablation was then determined from the difference between the expected and observed basal displacement. The approach used here is described in more detail in ref.[57].

Vertical displacements between profiles observed at the same site were quantified by cross-correlating overlapping 15 m segments of the profiles. This provided vertical displacement estimates at 7.5 m resolution throughout the ice shelf. First, the integer range-bin (or coarse) offset between the two profiles was determined by cross-correlation of the profile amplitude. Fine-scale offsets were determined from the mean phase difference between the profile segments. This was evaluated from the angle of the cross-correlation of the complex profile segments, after applying the coarse offset. The estimates of coarse and fine displacements were summed to provide an estimate of the total vertical displacement between the two profiles (Supplementary Fig. 1).

The displacement of the ice base was estimated in a similar manner. Amplitude cross-correlation was used to determine the coarse offset, and complex cross-correlation to determine the phase difference. The ice base was assumed to be the strongest peak in each profile, the coarse offset was determined using the 10 m segment of the first profile above the peak of the basal reflector. The phase difference was determined from the leading edge of the basal peak, defined here as the 1 m segment of the profile above the peak of the basal reflector.

The resulting estimates of vertical displacement throughout the profile were used to tune a model of displacement that was employed to estimate the expected location of the base. The displacement model was formed to allow for the major processes expected to influence the observations, namely hardware changes, accumulation, vertical strain and firn compaction. The model was of the form:

$$\delta z(z) = A + Bz + Ce^{(-z/z_0)} \qquad (1)$$

Here $\delta z(z)$ is the modelled vertical displacement of internal reflectors as a function of z, the range from the antenna calculated using a nominal propagation velocity of 1.68×10^8 m s^{-1}. A represents a range independent offset allowing for hardware changes and surface accumulation. B represents linear vertical strain, associated with horizontal convergence/divergence in the ice shelf. The third term on the right hand side represents an exponential model of firn compaction with surface compaction C, and length scale z_0. As many sites had insufficient depth to determine z_0 robustly, this was set to 21 m based on sites where this could be determined from the observations.

This model was used at all sites except the frontal site on Transect TB (tb_00000). Here, curvature in the deep displacement observations suggested bending, possibly caused by a submarine keel at the ice front[59], for example. To allow for this deformation, a more complex displacement model that also allows

for vertical displacement caused by bending of the ice shelf was used at this site as follows:

$$\delta z(z) = A + Bz + Ce^{(-z/z_0)} + D(z - z_n)^2 \qquad (2)$$

The final term here represents the vertical displacement induced by bending as a quadratic function of distance from neutral depth z_n, following ref.[60], and D represents the unknown model bending coefficient (m^{-1}).

The model free parameters at each site were tuned to minimize the model–observation differences in a least-squares sense, using nonlinear optimization. After tuning, the model was used to determine the displacement of the base expected in the absence of basal ablation. The melt rate was then determined from the difference between the observed and expected vertical displacement of the basal reflector and the observation interval (Supplementary Fig. 1).

Formal errors in the melt rate estimates are typically 0.01–0.1 m yr^{-1} (Supplementary Tables 1 and 2), usually dominated by the 1% uncertainty in the signal propagation speed in ice[58]. Systemic errors, such as the appropriateness of the firn compaction model, are unaccounted for in the formal error estimate; however, the results are (within the stated errors) robust to reasonable variations in processing methods.

Spatial interpolation of melt rates. To estimate net basal ablation from the survey region and to aid visualization of the melt rate field, the point-melt rate observations were interpolated onto a regular 1 km grid using the geostatistical interpolation method of kriging[61]. Kriging is typically used where the underlying value of the assumed stochastic process being sampled is either constant (simple kriging) or a linear function of position (kriging with a trend). However, in this case melt rate variability is a strong nonlinear function of frontal distance. To improve the statistical properties of the kriged variable, the observed melt rates (m_o) were first decomposed into a modelled component that includes a mean melt rate and a component of frontal melt enhancement (m_m), and a melt rate anomaly (m_a) (Supplementary Fig. 2), that is:

$$m_o(x, y, d) = m_m(d) + m_a(x, y) \qquad (3)$$

Here x and y are spatial coordinates, and d is the minimum distance to the ice front. Kriging was performed on the melt rate anomaly and after interpolation, the modelled component determined for the grid location was added to the interpolated anomaly. This approach is closely related to regression-Kriging[62]; however, in this case the explanatory variation (m_m) is a nonlinear function of the auxiliary variable (frontal distance).

Following ref.[34], frontal melt enhancement was modelled as an exponential function of frontal range. A spatially constant term was added to accommodate the non-zero melt rates apparent at sites furthest from the ice front, providing a melt rate model of the form:

$$m_m = \alpha + \beta e^{(-d/d_0)} \qquad (4)$$

Here α is a spatially constant background melt rate, β is the magnitude of melt rate enhancement at the ice front, d is the distance to the front of the RIS, and d_0 is a frontal effect length scale. Some frontal effect is evident on the MIS, but there are insufficient observations near the front of the MIS to reliably tune a model of frontal melt enhancement. Furthermore, differences in SST between the RIS ice front and McMurdo Sound (Fig. 3b) suggest that the frontal effects in the two regions are likely to vary. For these reasons, we do not model frontal melt enhancement for the MIS.

Least-squares fitting of the model to the 78 melt rate observations provided parameter estimates of $\alpha = 1.29 \pm 0.09$ m yr^{-1}, $\beta = 5.0 \pm 0.4$ m yr^{-1} and $d_0 = 1,900 \pm 300$ m. The model provides a good fit to the observations (Supplementary Fig. 2) with a coefficient of determination $R^2 = 0.78$, confirming that much of the melt rate variability within the network can be described by this simple model of frontal melt enhancement.

Kriging with a linear trend was implemented using the mGstat toolbox[63] for a spherical semi-variogram with a sill of 0.45 m^2 yr^{-2} and a range of 40 km; properties that are based on the observed spatial covariance of the melt rate anomaly (Supplementary Fig. 2). After kriging, the modelled melt rates (Supplementary Fig. 2) were added to the interpolated anomaly field (Supplementary Fig. 2) to produce the final gridded melt rate estimate (Fig. 1a). Kriging also provides an estimate of the variance of the interpolated value, and the resulting melt rate field was cropped to exclude land, sea and regions where the estimated standard deviation was >0.5 m yr^{-1}.

Mooring. The sub-ice shelf mooring was deployed on 21 January 2011 through a hot-water-bored access hole at 77° 29.315′ S, 171° 34.272′ E, approximately 7 km south of the ice front. Ice-shelf and water-column thicknesses at the deployment site were 266.5 m and 578 m, respectively, and the depth of the sea bed was 798.5 m. This deployment followed the two-month deployment discussed in ref.[31].

Nortek Aquadop current meters and Seabird SBE-37 T–S instruments were located at 4 levels throughout the water column from ~10 m below the ice base to ~30 m above the sea bed. Further details of the moored instrumentation and processing are provided in ref.[57].

The ULS was composed of an upward-looking Tritech PA-500 acoustic altimeter, configured as an external sensor to a Nortek Aquadop current meter and mounted on the mooring wire 15 m below the ice base. To avoid detecting the deployment borehole, the sensor was tilted 13° from the mooring wire, and its 5° acoustic beam width implies a ~2 m diameter acoustic footprint at the ice base. The instrument sampled every second hour from January 2011 until battery failure in December 2014.

The raw range record required substantial processing to remove outliers and noise. Processing included removing outliers and correcting for mooring swing, sensor tilt and sound speed variations. The remaining scatter in the range observations of ±0.15 m, attributed to basal roughness within the insonified region, was minimized by low-pass filtering of the time series with a cutoff frequency of 0.02 cycles d^{-1}. Radar observations at the mooring site provide a precise and independent measure of basal melting that can be used to validate the ULS estimate. Between observations on 16 January 2013 and 10 January 2014, the radar and ULS indicate mean melt rates of 1.57 ± 0.02 m yr^{-1} and 1.66 m yr^{-1}, respectively. The 0.09 m yr^{-1} discrepancy between the estimates is attributed to error in the ULS melt rate estimate. Further details of the instrument, processing and validation are given in ref. [57].

SST and sea ice concentration. SST data were downloaded from the Group for High Resolution Sea Surface Temperature (GHRSST) Multiscale Ultrahigh Resolution L4 archive[36]. The time series in Fig. 2c was produced from daily foundation SST fields at a nominal resolution of 5 km, averaged over the region within 100 km of the mooring. The spatial fields in Fig. 3 were derived from daily foundation SST fields at 25 km resolution, averaged over all January samples within the years 2003–2018. The mean sea-ice concentration time series in Fig. 2c and the monthly 15% sea ice concentration contours in Fig. 3a,b are derived from the 25 km resolution NOAA/NSIDC Climate Data Record of Passive Microwave Sea Ice Concentration, Version 3[42,56]. The time series was created from daily sea ice fields, averaged over the region within 100 km of the mooring. Contours were created from monthly mean fields averaged over the years 2010–2017. Daily and monthly datasets were downloaded from the National Snow and Ice Data Centre at ftp://sidads.colorado.edu/pub/DATASETS/NOAA/G02202_V3/south/.

Polynya surface heat content. To determine the available sensible heat content of the surface ocean layer within the polynya region in January, we estimated its mean properties as follows. For the 8.3×10^4 km^2 region within the 0 °C SST isotherm (Fig. 3b), the mean January SST is 0.22 °C. From the CTD cast in Fig. 2b, we assume a surface salinity of 34.4 psu. The freezing point potential temperature of this water at a depth of 200 m, typical of ice draft in the survey region (Fig. 1a), is −2.04 °C. This indicates a temperature difference between the surface layer and the ice base, or thermal driving[64], of 2.26 °C. Using a seawater density of 1,030 kg m^{-3}, this implies a thermal reservoir of 8.3×10^{17} J m^{-1} per metre of mixed layer. Archived CTD observations[65] indicate a wide range of mixed-layer thicknesses within this region during summer, typically exceeding 10 m. Assuming a mixed layer thickness of 10 m implies a surface layer sensible heat content of 8.3×10^{18} J. Using an ice density of 916 kg m^{-3}, and an initial temperature of −25 °C (indicative of surface temperatures in the region[25]), this heat is sufficient to melt 22 Gt of the ice shelf.

Data availability

Data for coastlines and ice shelves in Figs. 2 and 3 are from the Antarctic Digital Database (https://www.add.scar.org/). The RIS frontal line was modified to reflect recent changes in frontal position. MODIS images in Figs. 1a and 3c were sourced from the NSIDC Images of Antarctic Ice Shelves archive (http://nsidc.org/data/iceshelves_images/index_modis.html). SST data are from the GHRSST Multiscale Ultra-high Resolution (MUR) SST record, obtained from the NASA EOSDIS Physical Oceanography Distributed Active Archive Center at the Jet Propulsion Laboratory (https://doi.org/10.5067/GHGMR-4FJ01). Sea-ice concentration data are from the NOAA/NSIDC Climate Data Record of Passive Microwave Sea Ice Concentration, Version 3 (https://doi.org/10.7265/N59P2ZTG). Offshore CTD data are from the Calibrated Hydrographic Data from the Ross Sea acquired with a CTD during the RV *Nathaniel B. Palmer* expedition NBP1101 (2011) dataset (https://doi.org/10.1594/IEDA/317595), downloaded from http://www.marine-geo.org/tools/search/Files.php?data_set_uid=17595. Mooring data are archived at https://figshare.com/s/1c92fe8eb227b878e344. ApRES radar data are archived at https://figshare.com/s/1255b7d76ed69e015c3a.

Code availability

Computer code used to process the radar observations is available from the corresponding author on request.

References

57. Stewart, C. L. *Ice-Ocean Interactions Beneath the North-western Ross Ice Shelf, Antarctica.* PhD thesis, Univ. Cambridge (2018).
58. Fujita, S., Matsuoka, T., Ishida, T., Matsuoka, K. & Mae, S. A summary of the complex dielectric permittivity of ice in the megahertz range and its applications for radar sounding of polar ice sheets. *Phys. Ice Core Records* http://hdl.handle.net/2115/32469 (2000).
59. Reeh, N. On the calving of ice from floating glaciers and ice shelves. *J. Glaciol.* **7**, 215–232 (1968).
60. Jenkins, A., Corr, H. F., Nicholls, K. W., Stewart, C. L. & Doake, C. S. Interactions between ice and ocean observed with phase-sensitive radar near an Antarctic ice-shelf grounding line. *J. Glaciol.* **52**, 325–346 (2006).
61. Thomson, R. E. & Emery, W. J. *Data Analysis Methods in Physical Oceanography* 3rd edn (Newnes, 2014).
62. Hengl, T., Heuvelink, G. B. & Rossiter, D. G. About regression-kriging: from equations to case studies. *Comput. Geosci.* **33**, 1301–1315 (2007).
63. Hansen, T. M. mGstat: a geostatistical Matlab toolbox (2004); https://sourceforge.net/projects/mgstat/
64. Holland, D. M. & Jenkins, A. Modeling thermodynamic ice-ocean interactions at the base of an ice shelf. *J. Phys. Oceanogr.* **29**, 1787–1800 (1999).
65. Boyer, T. P. et al. *World Ocean Database 2013* (NODC, accessed 3 June 2016); https://www.nodc.noaa.gov/